Dalton Transactions

Accepted Manuscript

ROYAL SOCIETY OF CHEMISTRY

www.rsc.org/dalton

Article type: Full Paper

Probing Structural Variation and Multifunctionality in Niobium Doped Bismuth Vanadate Materials

Sameera Saithathul Fathimah, Padala Prabhakar Rao, Vineetha James, Athira K. V. Raj, Chitradevi G.R, Sandhyakumari Leela*

Materials Science and Technology Division
CSIR-National Institute for Interdisciplinary Science and Technology
Thiruvananthapuram
695019
India

E-mail: padala_rao@yahoo.com

Keywords: Bismuth vanadate, monoclinic, yellow color, methylene blue degradation, multifunctional material

Abstract

Multifunctional materials are developed in $BiV_{1-x}Nb_xO_4$ solid solutions via structural variation. Citrate gel route has been employed to synthesize these materials followed by calcination at various temperatures leading to fine particles. The effects of niobium doping over the structural variation and its influence on the optical properties are assessed by powder X-ray diffraction (XRD), Raman spectroscopy, scanning electron microscope (SEM), transmission electron microscope (TEM), UV-Vis-NIR spectroscopy. These solid solutions exhibit superior coloristic properties which are comparable to commercially available yellow pigment. These materials also show remarkable reflectance in the NIR region which makes them potential candidates for cool roof applications. Notable methylene blue dye degradation property is observed in Nb^{5+} doped $BiVO_4$ under sunlight irradiation.

1. Introduction

Visible light response of vanadate based colored compounds have attracted for a wide variety of applications.[1-5] Particularly bismuth vanadate ($BiVO_4$) has attracted wide attention because of its excellent physical and chemical properties, such as ionic conductivity,[6] ferroelasticity,[7] photochromicity,[8] gas sensing ability[9] etc. $BiVO_4$ is widely explored for its photocatalytic activity since it has response in visible region unless the widely known TiO_2 which has a major defect of being active in UV region only and thus reducing its performance in sunlight. $BiVO_4$ as a visible light driven photocatalyst has been studied extensively for the splitting of water,[10-12] the reduction of carbon dioxide into ethanol in water[13] and the elimination of organic pollutants such as methylene blue (MB),[14] methyl orange,[15] rhodamine,[16] etc under visible light irradiation. Since discharge of toxic dyestuff from the industries pose a serious threat to environment and health, sunlight driven degradation of these contaminants by photoresponsive materials provides a green technique for the elimination of toxic contaminants from the environment by its efficiency and broad pertinence. The band gap of $BiVO_4$ (2.4 eV)[17] allows favorable separation of e-h pairs which enhance its photoactivity. Also the non toxic behavior of $BiVO_4$ has made it a hot candidate especially for lead free paint applications.[18] However, $BiVO_4$ is very sensitive to factors such as synthesis techniques, resultant crystal structure and defect contents. So difficulty arises in controlling the photophysical properties of $BiVO_4$.

$BiVO_4$ exists in three crystal forms: monoclinic[19] (distorted scheelite structure, fergusonite structure), tetragonal[20] (scheelite structure) and tetragonal[21] (zircon type structure). The investigation results indicate that the visible light response of $BiVO_4$ strongly depends on its crystal form and morphology.[22-24] The properties, phase formation and morphology of $BiVO_4$ are related to the synthetic method, raw materials and reaction conditions.[25-26] Monoclinic

$BiVO_4$, when synthesized by high temperature route leads to irregular shape and large crystal size due to its rapid crystal growth feature. Therefore, the tendency to form a large number of defects, which are unfavorable for the photocatalytic performance, will be found in the products due to the volatilization of ions. Other methods include hydrothermal,[27] sol–gel,[28] coprecipation,[29] metallo organic deposition,[30] ultrasonic spray pyrolysis,[11] etc which results in nano sized particles. Also the aid of surfactants and other inorganic materials are utilized in these preparation procedures which are costly and limits its industrial applicability. Thus various efforts have been made to improve its properties by changing the synthesis conditions. $BiVO_4$ has been modified by noble metal loading,[31] cation[32] or anion[33] substitution or by combination with other oxide materials to form composites.[34] Structural substitution and solid solution formation[35-37] can improve band structure, efficient e–h separation and the morphological properties of the respective material, such as particle size or shape. In the present work, citrate gel route has been employed to synthesize Nb^{5+} doped $BiVO_4$ because it offers many advantages over conventional solid state method in the synthesis of fine powders, such as higher uniformity in particle size distribution, non agglomeration etc.

Transition metal cation doping may change the e-h behavior leading to changes in the electronic structure of the material.[38] The effect of various transition metals on $BiVO_4$ have been studied by DFT calculations.[39] According to this report, the solubility of Nb^{5+} is the highest in $BiVO_4$ host. Our group have been working on $BiVO_4$ based yellow pigments and attempted to improve its coloristic and NIR reflectance properties by various isovalent substitutions.[41-42] High NIR reflective pigments are now in great demand for the construction of cool roofs. A cool roof reflects radiations in the infrared region and results in less heat build-up thereby reducing cooling costs.[42] In this work, we report the multifunctional capability of $BiVO_4$ surpassing the color

performance of commercial $BiVO_4$ pigment, Sicopal Yellow L1100 by a citric acid complexation process. It can be found that materials with good stoichiometry and particle size can be synthesized. The as-obtained Nb^{5+} doped $BiVO_4$ materials exhibit enhanced photocatalytic dye degradation under sunlight irradiation thus possessing the potential for environmental and energy saving applications.

2. Experimental details

Samples $BiVO_4$, $BiV_{0.975}Nb_{0.025}O_4$, $BiV_{0.95}Nb_{0.05}O_4$, and $BiV_{0.925}Nb_{0.075}O_4$ were synthesized by the citrate gel method (CG). $Bi(NO_3)_3.5H_2O$, NH_4VO_3, $NbCl_5$ (Sigma Aldrich, 99.9% purity) were used as starting materials. Distilled water and citric acid (Sigma Aldrich, 99.9% purity) were used as solvent and chelating agent for the process. The citrate solution was prepared by dissolving appropriate amount of citric acid in distilled water. After complete homogenization of citrate solution, all the cationic solutions were dissolved in the citrate solution (1:2). The solution was kept for constant stirring for 1 h for homogenous mixing and concentrated by keeping it in the water bath (maintained at 100°C) for 12 h and the solution became viscous gel. The gel was dried to form a black product and then powdered by grinding in an agate mortar, which is the precursor. Then heat treatment of the precursor was carried out separately at various temperatures 300, 400 and 500°C for two hours respectively.

The calcined powders were characterized by means of X-ray powder diffraction (XRD) using a Ni filtered Cu-Kα radiation with a PANalytical X'pert Pro diffractometer operated at 45kV and 30mA fot its crysatlline structure. Data were collected from 10-70° 2θ range with a step size of 0.016°. The Raman spectra of the powder samples were acquired using an integrated micro-Infrared micro-Raman system using a 513 nm helium-neon laser operating at 10mW with a spatial resolution of 2μm. Particle morphological analysis of the powder was performed by means of a scanning electron microscope with JEOL JSM-5600 LV SEM with an acceleration

voltage of 15 kV. The TEM images and selected area electron diffraction (SAED) pattern of the samples were carried out on a FEI TECNAI 30G2 S-TWIN transmission electron microscope (TEM) operating at 300 kV. Energy dispersive analysis and elemental mapping of the samples was analyzed using Silicon Drift Detector–X-Max^N attached with a Carl Zeiss EVO SEM. EDS elemental mapping was conducted by AZtecEnergy EDS Microanalysis software. The UV visible spectra of the samples was measured with a UV–Vis–NIR spectrophotometer (Shimadzu, UV-3600) using $BaSO_4$ as a reference. Optical measurements were performed in the 220 to 800 nm wavelength range. The measurement conditions were as follows: an illuminant D65, 10° complementary observer and measuring geometry d/8°. The color coordinates were determined by coupling analytical software (UVPC Color Analysis Personal Spectroscopy Software V3, Shimadzu) to the UV–3600 spectrophotometer. The color of the pigments was evaluated according to The Commission Internationale del' Eclairage (CIE) through $L^*a^*b^*$ 1976 color scales (CIE-LAB 1976 color scales). In this system L^* is the color lightness (L^* is zero for black and L^* is 100 for white), a^* is the green (-)/ red (+) axis, and b^* is the blue (-)/yellow (+) axis. The parameter C^* (chroma) represents saturation of the colour and h^0 represents the hue angle. The chroma is defined as $C* = \sqrt{(a*)^2 + (b*)^2}$. The hue angle, h^0 is expressed in degrees and ranges from 0° to 360° and is calculated using the formula $h^0 = \tan^{-1}\left(\frac{b^*}{a^*}\right)$. The near–infrared reflectance of the powdered pigment samples was measured with a UV–Vis–NIR spectrophotometer (Shimadzu, UV–3600 with an integrating sphere attachment) using poly–tetrafluoroethylene (PTFE) as a reference in the 700 to 2500 nm range. The NIR solar reflectance in the wavelength range from 700 to 2500 nm was calculated in accordance with the ASTM standard number G173-03. The NIR solar reflectance is expressed as the integral of the percent

reflectance times the solar irradiance divided by the integral of the solar irradiance when integrated over the 700-2500 nm range as shown in the formula,

$$R = \frac{\int_{700}^{2500} r(\lambda) i(\lambda) d\lambda}{\int_{700}^{2500} i(\lambda) d\lambda}$$

where r(λ) is the spectral reflectance obtained from the experiment and i(λ) is the standard solar spectrum (Wm^{-2} mm^{-1}) obtained from the standard. The Brunauer-Emmet-Teller (BET) surface area of the materials were analysed by nitrogen adsorption – desorption measurement using Micrometrics Tristar Surface Area Analyser.

The photocatalytic activity of samples, processed via citrate gel route, was studied by monitoring the degradation of methylene blue dye in an aqueous suspension containing the samples under continuous solar-radiation exposure and magnetic stirring. All photocatalytic experiments were carried out under similar conditions in the city of Thiruvananthapuram (latitude: 8.460 N; longitude: 76.980 E), (India). All the solar experiments were performed on an average light intensity of 8 x 10^4 lux in order to avail maximum sunlight. A 75 mL of aqueous suspension was prepared by mixing 1x10^{-5} M dispersing 0.02 g of the samples in the de-ionized water. The resulting suspension was equilibrated by stirring in dark for 20 min to stabilize the adsorption of MB dye on the surface of samples. The stable aqueous suspension was then exposed to natural sunlight. Following sunlight exposure, 8 mL of aqueous suspension was taken out of suspension after each 20 min interval for total 160 min of sunlight exposure for obtaining the absorption spectra. The degraded solution of MB was analyzed by a UV-visible spectrophotometer (Hitachi 3900H) and the absorption peak at 664 nm was monitored.

The organic intermediates obtained at various intervals were analyzed by the high-pressure liquid chromatography and gas chromatography mass spectrometry (HPLC and GC–MS) method. The degradation products were characterized by a GCMS-QP2010 (SHIMADZU Corporation, Japan). The organic intermediates produced during degradation, were extracted with equal volumes of ethyl acetate and directly used for further study. GC conditions included split injection mode with carrier gas Helium and MS conditions included an ion source temperature of 200^0C.

3. Results and discussion

From the powder XRD patterns analysis of $BiVO_4$, $BiV_{0.975}Nb_{0.025}O_4$, $BiV_{0.95}Nb_{0.05}O_4$ and $BiV_{0.925}Nb_{0.075}O_4$ calcined at 300, 400 and 500°C, it is seen that the samples calcined at 500°C are the most crystalline in nature. Fig. 1a shows the powder X-ray diffraction patterns of samples calcined at 500°C. All the reflections are indexed as per the monoclinic scheelite (s-m) phase with a space group $I_{2/b}$ and the reflections can be well indexed according to the powder diffraction file no. 01-083-1699. As said earlier, $BiVO_4$ has three main crystal forms: zircon-structure with tetragonal system and scheelite structure with monoclinic and tetragonal systems. The crystal structure of monoclinic scheelite $BiVO_4$ is much similar to that of tetragonal scheelite, except for the distortion.[43] The Bi–O polyhedron in the former is more distorted than that of tetragonal scheelite $BiVO_4$ due to the presence of a $6s^2$ lone pair of Bi^{3+}. The difference in the XRD patterns between $BiVO_4$ (s-m) and $BiVO_4$ (s-t) can be judged by the existence of a peak at 15° and splitting of peaks at 18.5°, 35°, and 46° of 2θ.[22] It is, therefore convenient to distinguish monoclinic and tetragonal scheelite $BiVO_4$ from XRD patterns. It is observed that on progressive doping with Nb^{5+}, the splitting of peaks at 18.5°, 35°, and 46° of 2θ are decreasing. Typical zoomed prominent peak position around 2θ 18° is shown in Fig. 1b and also provided a

graph showing the variation of the peak split width upon Nb^{5+} doping (Inset of Fig.1b). This graph reveals a linear decreasing trend of the peak split width upon Nb^{5+} doping. These results suggest that the progressive doping of Nb^{5+} induces a structural variation from monoclinic scheelite to tetragonal scheelite type.

The crystalline nature of the phases is evident from powder diffraction patterns which suggests that all the samples on Nb^{5+} doping form solid solutions in $BiVO_4$. The structure is constructed by VO_4 tetrahedron and BiO_8 dodecahedron structural units. The V site is bordered by four oxygen atoms forming a VO_4 tetrahedron and the Bi site too by eight oxygen atoms making a BiO_8 dodecahedron. The slightly distorted feature comes from the fact that there are four types of Bi-O bonds and two types of V-O bonds.[44] The ionic radii of Bi^{3+} in eight fold coordination is 0.117 nm and V^{5+} in four fold coordination is 0.035 nm and doping Nb^{5+}(0.048 nm)[45] into V^{5+} will cause slight distortion in the VO_4 tetrahedron and BiO_8 dodecahedron of the lattice as obvious by difference in ionic radius.

The crystallite size is calculated from the Debye Scherrer formula [46]

$$D=0.9\lambda/\beta\cos\theta, \quad (1)$$

where D is the crystallite size, λ is the wavelength of X-ray used, β and θ are the half width of the X-ray diffraction lines and half diffraction angle 2θ. The instrumental broadening was rectified using silicon as the external standard. The crystallite size of $BiVO_4$ is found to be in the range 74-123 nm at various temperatures (300-500°C). On doping with Nb^{5+}, a reduction in crystallite size is observed. The crystallite size obtained at various temperatures is given in Table 1. The strain induced in the lattice is estimated using Williamson-Hall (W-H) method where both size-induced and strain-induced broadening are deconvoluted by considering the peak width as a

function of 2θ. According to W-H method, the width of individual reflections can be expressed as follows:[47]

$$\beta\cos\theta = \frac{K\lambda}{D} + 4\varepsilon \sin\theta \quad (2)$$

where β is the width of peaks, D is the crystallite size, λ is the wavelength of Cu Kα radiation and ε is the crystal strain effect. A plot is drawn with 4sinθ along the x-axis and β_{hkl} cosθ along the y-axis. From the linear fit to the plot, the strain ε was determined from the slope of the fit. The lattice strain induced in $BiV_{0.975}Nb_{0.025}O_4$ synthesized at 500°C is 0.31 % whereas in $BiVO_4$ it is about 0.18% (Fig. 2). It is observed that on doping, as crystallite size decreases lattice strain increases (Table 1). It is obvious from W-H plot that on Nb^{5+} doping, atomic shifts might have induced some strain in $BiVO_4$ lattice which may be responsible for the enhancement of color as discussed in the latter part of the section.

Raman scattering spectra of the samples calcined at 500°C, was performed to understand its local structure (Fig. 3). To identify more accurately the peak positions, we fitted the Raman spectra using Lorentz function. Typical Lorentz fits are provided in the supporting information (Figure S1 ESI).The Raman spectra shows characteristic bands of monoclinic scheelite structure in agreement with the literature.[48-49] In this regard, the 218 cm^{-1} band was the external mode of $BiVO_4$, which gave little structural information. The Raman bands at 337 (B_g anti-symmetry) and 372 cm^{-1} (A_g symmetry) were assigned to the asymmetric and symmetric deformation modes of the VO_4^{3-} tetrahedron, respectively. Meanwhile, the most intense Raman band at about 813 cm^{-1} (A_g symmetry) was assigned to the symmetric V-O stretching mode. The shifts of Raman band at 813 cm^{-1} (V-O stretching vibration) to lower frequency indicate increasing V-O bond distance corresponding to the shorter bond length. This increase of shorter bond length improves the symmetry of VO_4 tetrahedra and further evidences a state of structural variation of

monoclinic to tetragonal phase. The V-O bond lengths are affected by position of bismuth ions and correlates with the variations occuring in the unit cell.[50] A functional relationship exists between the Raman stretching frequency ν and the metal-oxygen bond length R in the local structure.[51-52]

$$\nu\ cm^{-1} = 21349 \exp(-1.9176\ R\ \text{Å}) \quad (3)$$

The FWHM obtained from Lorenzian peak fitting for x = 0, 0.025, 0.050, 0.075 are 69.7, 83.1, 81.7, 75.6 respectively. This indicates that there is heterogenity with respect to the local strain induced in doped samples and the highest variation is seen for x= 0.025 which may be the reason for the enhancement of color in samples. A continuous shift of this Raman band to lower wavenumbers, from 813 to 811 cm^{-1} reveals that the average short-range symmetry of the VO_4 tetrahedra becomes more regular. The shifting of the corresponding symmetric V-O stretching mode in Nb^{5+} doped $BiVO_4$ (m-s) towards lower wavenumber leads to increase in bond length from 1.7044 (Å) to 1.7052 (Å). The variations induced in $BiVO_4$ unit cell is evident from Raman analysis. Thus it is evident that slight change in the V-O bond length may be responsible for the enhanced photoresponse of the samples.

The homogeneous and crystalline nature of the samples can also be observed in the SEM photographs (Fig. 4). The samples have a particle size of about 100 nm when synthesized at 300°C and the particle size is increased to about 400 nm at 500°C. There is a slight increase in particle size upon Nb^{5+} doping. From the micrographs it is clear that the particles texture is smooth and somewhat spherical in nature and they are distributed uniformly.

EDS analysis of samples confirm that the samples are composed of Bi, V, Nb and O in the appropriate ratio. Elemental X-ray dot mapping analysis of typical $BiV_{0.975}Nb_{0.025}O_4$ pigment calcined at 500°C confirms that niobium ions are uniformly distributed in $BiVO_4$ lattice (Fig. 5).

TEM images of the samples calcined at 500°C reveals that particles are a bit aggregated (Fig. 6). TEM investigation confirms the particle diameter in the size range of 100–300 nm and the SAED patterns indicate that they are polycrystalline. TEM confirms that particle size is slightly affected by niobium doping.

The absorption spectra of the $BiVO_4$, $BiV_{0.975}Nb_{0.025}O_4$, $BiV_{0.95}Nb_{0.05}O_4$, $BiV_{0.925}Nb_{0.075}O_4$ synthesized at 500°C, represented with Kubelka-Munk absorption function, $f(R) = (1-R)^2/2R$, where R is the reflectance (Fig. 7). The colors of the samples are bright yellow and possess steep absorption edge in the visible light region. The steep absorption edge means that the visible light absorption is due to the band-gap transition.[53] It is well known that the band-gap transition of $BiVO_4$ is formed by charge-transfer from the hybrid orbitals of Bi6s and O2p to V3d orbitals. As a crystalline semiconductor, the optical absorption near the band edge follows the formula:[54]

$$\alpha h\nu = A(h\nu - Eg)^{n/2} \quad (4)$$

where α, ν, Eg and A are absorption coefficient, light frequency, band gap and a constant, respectively. Among them, n depends on the characteristics of the transition in a semiconductor, i.e. direct transition (n = 1) or indirect transition (n = 4). For $BiVO_4$, the value of n is 1.[55] The band gap energy (Eg value) of $BiVO_4$ can thus be estimated from a plot $(\alpha h\nu)^2$ versus photon energy (hν). The intercept of the tangent to the x-axis will give a good approximation of the band gap energy for the samples. Tauc plots of the $(\alpha h\nu)^2$ versus photon energy (hν) of samples at 500°C are shown in supplementary information (Figure S2 ESI). The addition of Nb^{5+} resulted in slight variations in band gap. The band gap energy of $BiVO_4$ can be calculated as 2.44 to 2.51 eV from Tauc plots, which means they have suitable band gaps for photocatalytic decomposition of organic contaminants under sunlight irradiation. The band gap energies of each samples were

found to decrease with increasing synthesis temperature. For samples synthesized at 300-500°C, on increase of dopant content it is seen that the band gap increases for $x = 0.025$ and then gets slightly decreased again. The estimated band gap energies of the samples are given in Table 2.

Thus there is a slight variation observed in the electronic structure of the samples when Nb^{5+} is doped into $BiVO_4$, thereby the distortion of the VO_4^{3-} tetrahedron occurs. This distortion is due to the lone pair electron of Bi^{3+} in the local structure of the $BiVO_4$. There may be a change in the extent of overlapping of Bi6s and O2p with the inclusion of Nb 4d orbitals. This overlapping is directly proportional to the degree of distortion which in turn helps in the mobility of photogenerated holes.

The color coordinates of the $BiV_{1-x}Nb_xO_4$ ($x = 0$, 0.025, 0.05, 0.075) pigments are given in Table 2. All the samples are yellow as the hue falls in the yellow region of the color space. The b^* value increases with each doping concentrations with increase in synthesis temperature. On increase of calcination temperature, the shades shift from greenish yellow to reddish yellow. The samples calcined at 500°C are reddish yellow while the lower temperatures yield greenish yellow. The samples calcined at 500°C shows an increment in b^* value from 71 to 89 upon Nb^{5+} doping (0.025). Further doping results in a slight decrease in b^* value up to 80. The enhancement in color may be due to the increased lattice strain imposed on $BiVO_4$ through Nb^{5+} doping. Thus the samples calcined at 500°C exhibit better yellow colors. The b^* value obtained for $x = 0.025$ is higher than commercial $BiVO_4$ (Sicopal Yellow L1100). [56] This implies the potential utility of the developed pigments for coloring applications.

The NIR reflectance spectra of $BiV_{1-x}Nb_xO_4$ ($x = 0$, 0.025, 0.05, 0.075) samples synthesized at 500°C are given in Fig. S3 ESI. It is seen that the pigments calcined at 500°C shows the highest NIR reflectivity compared to lower synthesis temperatures. $BiVO_4$ synthesized

by citrate gel route possesses an NIR reflectance of 61% in the 1100 nm range. Doping of Nb^{5+} into $BiVO_4$ enhances the NIR reflectance to 86 % for x = 0.025. For x greater than 0.025 a slight decrease in values up to 68% is observed. The NIR solar reflectance spectra determined in accordance with ASTM Standard G173-03[57] of powdered samples are presented in Fig. S4 ESI. The enhancement of the optical properties of $BiVO_4$ is mainly ascribed to the reduction in crystallite size and structural variation in the lattice. The high NIR reflectance displayed by all the newly obtained yellow colored samples makes them interesting candidates for use as cool colorants.

Temporal changes in the concentration of MB were monitored by examining the variations in maximal absorption in UV–Vis spectra at 664 nm. In the presence of the photocatalyst and visible light irradiation, the degradation of MB obviously increased. It can be found that the doping of Nb^{5+} affects the photocatalytic activity of $BiVO_4$. Fig. 8 shows the temporal absorption spectral patterns of MB during the photo degradation process in typical $BiV_{0.95}Nb_{0.05}O_4$ sample synthesized at 500°C. The typical sample shows the highest degradation activity. Photocatalytic efficiency (C) of samples was calculated by the following equation,

$$C = (A_0 - A)/A_0 \times 100\%, \quad (5)$$

where A_0 is the absorbance of its maximum absorbance wavelength, A is the absorbance at the same wavelength of extracted solution. For x = 0, C was found to be 81, for x = 0.050 it was 88. The absorption peak gradually shifted from 664 nm to 616 nm with a decrease in absorption during the process of photocatalytic degradation. Such a blue-shift is characteristic process of N-demethylation derivatives of MB. With the photocatalytic degradation of MB, the absorption peak at 664 nm disappeared due to the formation of a mixture of N-demethylated analogs (Azure B, Azure A, Azure C and Thionine) of MB.[58-59] This result suggested that demethylation process

was likely to be a major step in the photocatalytic oxidation of MB. As a direct electron transition semiconductor, the monoclinic $BiVO_4$ is excited by the incident photons with energy equal to or greater than their band energy level. Electrons and holes that migrate to the surface of the semiconductor without recombination can respectively reduce or oxidize the reactants adsorbed by the semiconductor. In the process of migration to the surface of the semiconductor, the mobility of the photo-generated charge carriers is a key factor. In general, charge separation and transfer of photogenerated electrons and holes are strongly affected by the crystal structural features of the materials, namely, crystallinity, defects, and any crystal structure distortion. Additionally, surface properties such as particle size, surface area, surface structure, and active reaction sites, which are mainly related to the morphology of the materials, are also important.

With the increase of the doping concentration (x = 0.075), the activity decreases as the tendency of structural variation to teragonal scheelite as obvious from the X-ray diffraction patterns as seen earlier. The dopant addition may cause variations in VO_4 tetrahedron which is favorable for the separation of photo-excited e-h pairs. Also, change in the electronic structures vary the degree of delocalization of photogenerated e-h pairs and leads to change in photocatalytic activity. The results show that upto x = 0.05 doping of Nb^{5+} shows enhanced photocatalytic activity than the undoped sample. When the doping percentage is increased, photocatalytic property decreases, due to the tendency to shift the structure from monoclinic to tetragonal. The surface area also gets increased from 1.08 m^2/g for undoped to 2.72 m^2/g for x = 0.05 doping of Nb^{5+}. This implies that increase in surface area too might have contributed to an increased photocatalytic activity.

Fig. S5 ESI shows a MS chromatogram obtained after MB degradation after 160 min of irradiation using $BiV_{0.95}Nb_{0.05}O_4$ photocatalyst. The direct ESI mass spectrum is shown in Fig.S

6 which shows main two peaks at retention time of 3.95 and 14.96 for MB. The two products identified in GC–MS spectra are at 256 m /z and 135 m/z. These can be assigned to the chemical structures Azure A[60] and thiophene.[61] Also many peaks with different intensities were observed in addition to MB dye suggesting that new products are formed in the course of degradation.This shows the complexity of the photocatalytic process.

Further HPLC analysis was also conducted to identify more organic intermediates using a Thermoscientific Q-Exactive ESI-HPLC MS instrument. The degraded MB samples collected at various intervals were dissolved in equal amounts of HPLC grade methanol and used for analysis. The formation of Azure C (m/z=242.2) was confirmed by HPLC analysis. Also phenothiazin could be detected at m/z= 200 from thionin deamination.[60] Thus GCMS and HPLC analysis confirmed the photodegradation of MB by forming various organic intermediates.Total organic carbon (TOC) was analyzed with an Liqui TOC II analyzer (elementar,Germany). Prior to injection into the TOC analyzer, the samples were centrifuged to remove any catalyst particles. The results showed that 65 % and 70% of TOC could be removed within 160 min of sunlight irradiation when $BiVO_4$ and $BiV_{0.95}Nb_{0.05}O_4$ were used as photocatalyst.TIC content remained constant throughout the reaction indicating no formation of any harmful substances in the photodegradation process.

4. Conclusions

Multifunctional novel non-toxic materials in $BiV_{1-x}Nb_xO_4$ system are reported for the first time. The fine particles are prepared by citrate complexation route. The pigments exhibit excellent color characteristics comparable to commercial $BiVO_4$. Also the high NIR reflectance of these pigments indicates their potential for cool roof applications. The high photon absorption capability of these materials is seen by considerable MB dye degradation property.

Acknowledgements

One of the authors, Sameera S. would like to acknowledge Council of Scientific and Industrial Research (CSIR), Govt. of India, for the financial support towards a Senior Research Fellowship. The authors thank Defense Research Development Organization (DRDO), Govt. of India, for the partial support.

References

1. H. Xie, T. Tsuboi, W. Huang, Y. Huang, L. Qin, H. J. Seo, *J. Am.Ceram. Soc*. 2014**,** **97**, 1434.
2. J. Liu, L. Wang, X. Sun, X. Zhu, *Angew. Chem.Int. Edit*. 2010, **49**, 3492.
3. M. Feng, L.-B. Luo, B. Nie, S.-H. Yu, *Adv.Funct. Mater*. 2013, **23**, 5116.
4. M. R. Dolgos, A. M. Paraskos, M. W. Stoltzfus, S. C. Yarnell, P. M. Woodward, *J.Solid State Chem*. 2009, **182**, 1964.
5. J. Xu, C. Hu, Y. Xi, C. Peng, B. Wan, X. He, *Mater. Res.Bull*. 2011, **46**, 946.
6. I. C. Vinke, J. Diepgrond, B. A. Boukamp, K. J. de Vries, A. J. Burggraaf, *Solid State Ionics* 1992, **57**, 83.
7. J. D. Bierlein, A. W. Sleight, *Solid State Commun*. 1975, **16**, 69.
8. A. Tücks, H. P. Beck, *Dyes Pigments* 2007, **72**, 163.
9. Y. Zhao, Y. Xie, X. Zhu, S. Yan, S. Wang, *Chem. Eur. J*. 2008, **14**, 1601.
10. A. Iwase, A. Kudo, *J. Mater. Chem*. 2010, **20**, 7536.
11. S. S. Dunkle, R. J. Helmich, K. S. Suslick, *J. Phys. Chem. C*. 2009, **113**, 11980.
12. W. J. Jo, J.-W. Jang, K.-j. Kong, H. J. Kang, J. Y. Kim, H. Jun, K. P. S. Parmar, J. S. Lee, *Angew. Chem. Int. Ed*. 2012, **51**, 3147.
13. Y. Liu, B. Huang, Y. Dai, X. Zhang, X. Qin, M. Jiang, M.-H. Whangbo, *Catal. Commun*. 2009, **11**, 210.

14. G. P. Nagabhushana, G. Nagaraju, G. T. Chandrappa, *J. Mater. Chem. A*. 2013, **1**, 388.

15. H. Li, G. Liu, X. Duan, *Mater. Chem. Phys*. 2009, **115**, 9.

16. Y. Zhang, G. Li, X. Yang, H. Yang, Z. Lu, R. Chen, *J. Alloys Compd*. 2013, **551**, 544.

17. A. Kudo, K. Omori, H. Kato, *J. Am. Chem. Soc*. 1999, **121**, 11459.

18. H. Endriss, in *High Performance Pigments*, Wiley-VCH Verlag GmbH & Co. KGaA, 2009, **7**.

19. J. Liu, H. Wang, S. Wang, H. Yan, *Mater. Sci. Eng*., **B** 2003, **104**, 36.

20. L. Hoffart, U. Heider, R. A. Huggins, W. Witschel, R. Jooss, A. Lentz, *Ionics* 1996, **2**, 34.

21. A. K. Bhattacharya, K. K. Mallick, A. Hartridge, *Mater. Lett*. 1997, **30**, 7.

22. T. Saimi, K. Hideki, K. Akihiko, *Chem. Mater*. 2001, **13**, 4624.

23. H.-q. Jiang, H. Endo, H. Natori, M. Nagai, K. Kobayashi, *J. Eur. Ceram. Soc*. 2008, **28**, 2955.

24. Z. Zhu, J. Du, J. Li, Y. Zhang, D. Liu, *Ceram. Int*. 2012, **38**, 4827.

25. P. Wood, F. P. Glasser, *Ceram. Int*. 2004, **30**, 875.

26. E. G. van der Linden, L. F. B. Malta, M. E. Medeiros, *Dyes Pigments* 2011, **90**, 36.

27. H. Fan, D. Wang, L. Wang, H. Li, P. Wang, T. Jiang, T. Xie, *Appl. Surf. Sc*i. 2011, **257**, 7758.

28. M. Wang, Q. Liu, Y. Che, L. Zhang, D. Zhang, *J. Alloys Compd*. 2013, **548**, 70.

29. U. M. García-Pérez, S. Sepúlveda-Guzmán, A. Martínez-de la Cruz, *Solid State Sci.* 2012, **14**, 293.

30. A. Galembeck, O. L. Alves, *J. Mater. Sci*. 2002, **37**, 1923.

31. P. Chatchai, S.-y. Kishioka, Y. Murakami, A. Y. Nosaka, Y. Nosaka, *Electrochim. Acta* 2010, 55, 592.

32. W. Luo, J. Wang, X. Zhao, Z. Zhao, Z. Li, Z. Zou, *PCCP* 2013, **15**, 1006.

33. H. Jiang, H. Dai, J. Deng, Y. Liu, L. Zhang, K. Ji, *Solid State Sci*. 2013, **17**, 21.

34. L. Zhang, G. Tan, S. Wei, H. Ren, A. Xia, Y. Luo, *Ceram. Int*. 2013, **39**, 8597.

35. M. Dragomir, I. Arčon, S. Gardonio, M. Valant, *Acta Mater*. 2013, **61**, 1126.

36. W. Yao, J. Ye, *J. Phys. Chem. B* 2006, **110**, 11188.

37. S. F. Sameera, P. P. Rao, L. S. Kumari, P. Koshy, *Chem. Lett*. 2009, **38**, 1088.

38. H. S. Park, K. E. Kweon, H. Ye, E. Paek, G. S. Hwang, A. J. Bard, *J. Phys. Chem. C*. 2011, **115**, 17870.

39. Z. Zhao, W. Luo, Z. Li, Z. Zou, *Phys. Lett. A* 2010, **374**, 4919.

40. S. F. Sameera, P. P. Rao, L. S. Kumari, V. James, S. Divya, *Chem. Lett*. **2013**, **42**, 521.

41. L. Sandhya Kumari, P. Prabhakar Rao, A. Narayana Pillai Radhakrishnan, V. James, S. Sameera, P. Koshy, *Sol. Energy Mater. Sol. Cells* 2013, **112**, 134.

42. H. Akbari, M. Pomerantz, H. Taha, *Sol. Energy* 2001, **70**, 295.

43. W. I. F. David, A. M. Glazer, A. W. Hewat, *Phase Transitions* 1979, **1**, 155.

44. Z. Zhao, Z. Li, Z. Zou, *Phy.Chem.Chemical Phys.* 2011, **13**, 4746.

45. R. Shannon, *Acta Crystallogr., Sect. A* 1976, **32**, 751.

46. J. I. Langford, A. J. C. Wilson, *J. Appl. Crystallogr*. 1978, **11**, 102.

47. A. Khorsand Zak, W. H. Abd. Majid, M. E. Abrishami, R. Yousefi, *Solid State Sci*. 2011, **13**, 251.

48. R. L. Frost, D. A. Henry, M. L. Weier, W. Martens, *J. Raman Spectrosc*. 2006**, 37**, 722.

49. F. D. Hardcastle, I. E. Wachs, H. Eckert, D. A. Jefferson, *J. Solid State Chem*. 1991, **90**, 194.

50. J. Yu, A. Kudo, *Adv. Funct. Mater*. 2006, **16**, 2163.

51. F. D. Hardcastle, I. E. Wachs, *J. Phys. Chem* 1991, **95**, 5031.

52. I. D. Brown, K. K. Wu, *Acta Crystallogr., Sect. B* 1976, **32**, 1957.

53. A. Walsh, Y. Yan, M. N. Huda, M. M. Al-Jassim, S.-H. Wei, *Chem. Mater*. 2009, **21**, 547.

54. M. A. Butler, *J. Appl. Phys*. 1977, **48**, 1914.

55. L. Zhou, W. Wang, S. Liu, L. Zhang, H. Xu, W. Zhu, *J. Mol. Catal. A: Chem*. 2006, **252**, 120.

56. Wendusu, T. Honda, T. Masui , Nobuhito Imanaka, *RSC Adv.*, 2013, **3**, 24941.

57. *ASTM International*, West Conshohocken,PA **2012**.

58. T. Zhang, T. Oyama, A. Aoshima, H. Hidaka, J. Zhao, N. Serpone, *J. Photochem. Photobiol., A* **2001**, 140, 163.

59. T. Zhang, T. k. Oyama, S. Horikoshi, H. Hidaka, J. Zhao, N. Serpone, *Sol. Energy Mater. Sol. Cells* 2002, **73**, 287.

60. M.A. Rauf, M.A.Meetani, A.Khaleel, A.Ahmed, *Chem. Eng. J.*,2010, **157**,373-378.

61. F. Huang, L. Chen, H. Wang, Z. Yan, *Chem. Eng. J.*, 2010,**162**, 250–256.

Table 1. Crystallite size and lattice strain of $BiV_{1-x}Nb_xO_4$ (x = 0, 0.025, 0.05, 0.075) synthesized at different temperatures.

Sample	Crystallite size (nm)			Lattice strain (%)		
	300°C	400°C	500°C	300°C	400°C	500°C
$BiVO_4$	74	77	123	0.14	0.17	0.19
$BiV_{0.975}Nb_{0.025}O_4$	49	53	91	0.37	0.33	0.35
$BiV_{0.95}Nb_{0.05}O_4$	46	51	87	0.26	0.34	0.30
$BiV_{0.925}Nb_{0.075}O_4$	40	57	77	0.22	0.29	0.29

Table 2. Color coordinates and band gap energies of $BiV_{1-x}Nb_xO_4$ (x = 0, 0.025, 0.05, 0.075) synthesized at different temperatures.

Calcination	composition	*L*	*a**	*b**	C*	h^0	Eg (eV)
300°C	x=0	71.52	-3.6	65.21	65.31	93.17	2.49
	x=0.025	65.58	-5.07	58.02	58.25	95	2.51
	x=0.050	62.56	-3.75	54.42	54.55	93.96	2.48
	x=0.075	48.37	-3.88	35.59	35.8	96.26	2.48
400°C	x=0	77.23	-2.79	72.0	72.06	92.23	2.46
	x=0.025	82.49	-3.0	82.33	82.39	92.1	2.49
	x=0.050	71.97	-3.88	65.37	65.49	93.41	2.46
	x=0.075	70.27	-3.36	63.56	63.65	93.04	2.44
500°C	x=0	77.18	-0.53	71.19	71.19	90.44	2.45
	x=0.025	85.99	0.93	89.29	89.29	89.4	2.48
	x=0.050	83.99	2.49	85.54	85.54	8.32	2.46
	x=0.075	79.72	1.64	80.13	80.13	88.82	2.44
	Sicopal Yellow[56]	94.4	-16.7	76.9			

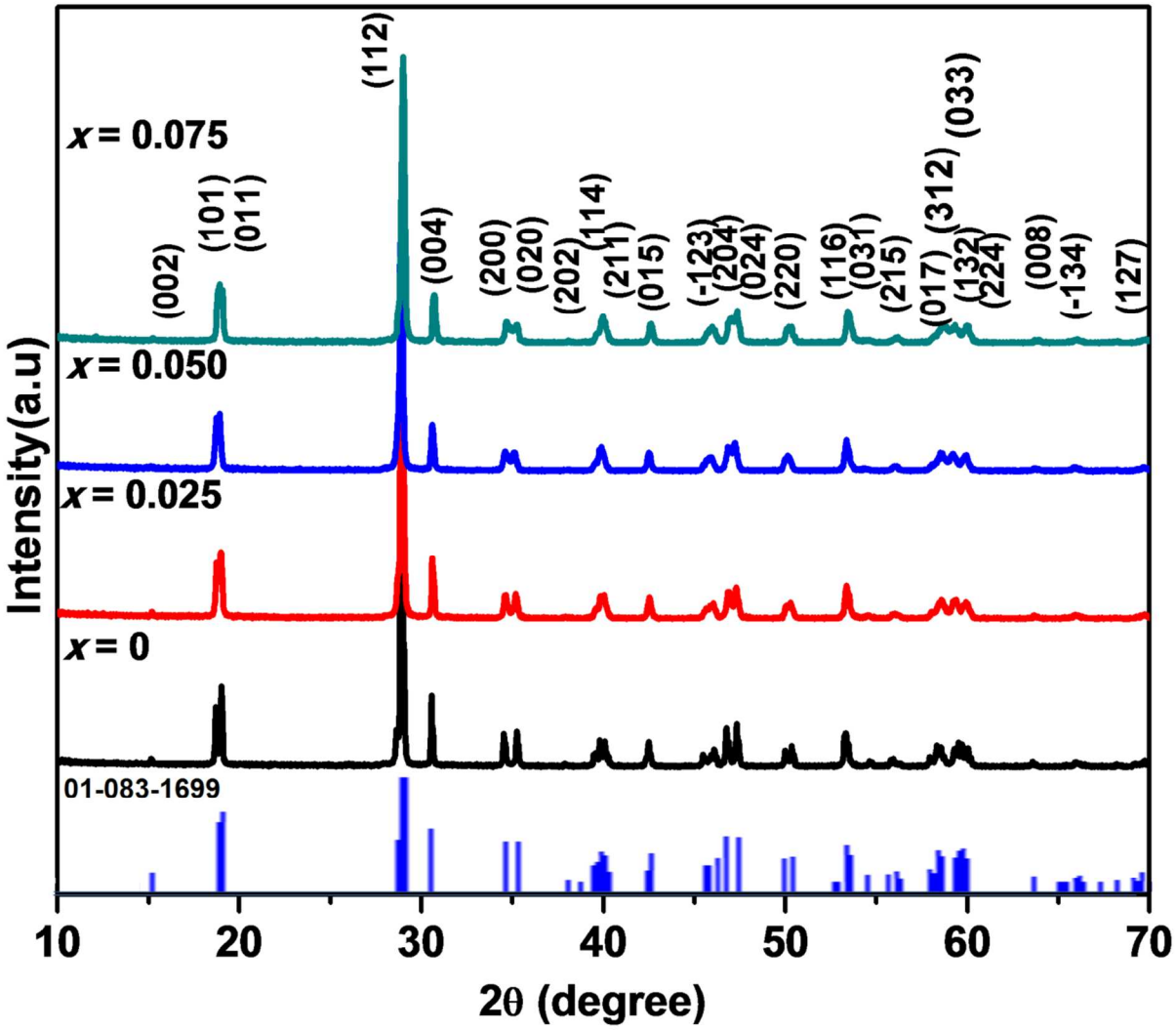

Fig. 1a Powder XRD patterns of $BiV_{1-x}Nb_xO_4$; $x = 0, 0.025, 0.05, 0.075$ synthesized at 500°C.

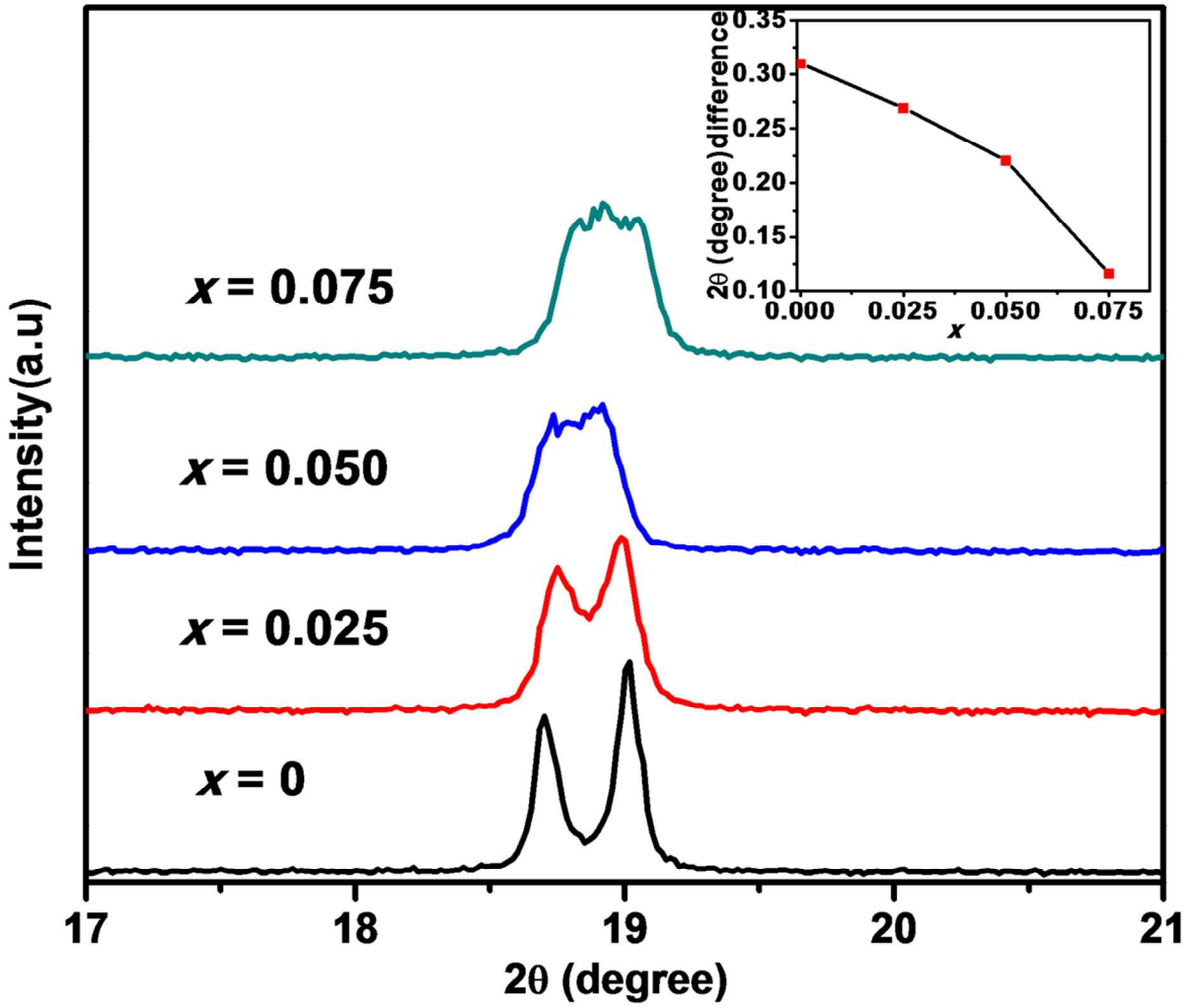

Fig. 1b Zoomed peak position of the characteristic monoclinic peak around 2θ 18° for the XRD patterns of $BiV_{1-x}Nb_xO_4$; $x = 0, 0.025, 0.05, 0.075$ synthesized at 500°C. (Inset shows variation of the peak split width with Nb^{5+} substitution.)

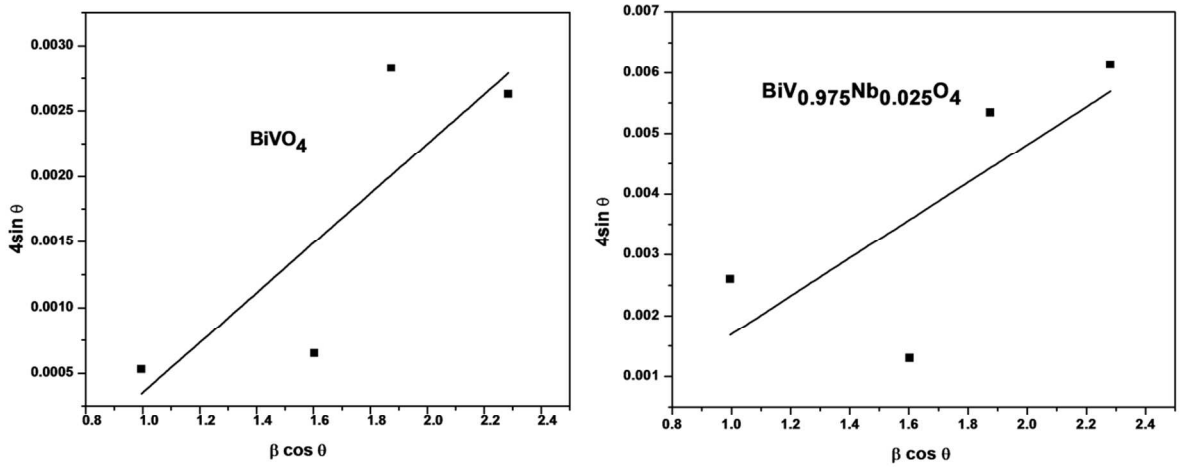

Fig. 2 W-H plots of $BiV_{1-x}Nb_xO_4$; x = 0, 0.025 synthesized at 500°C.

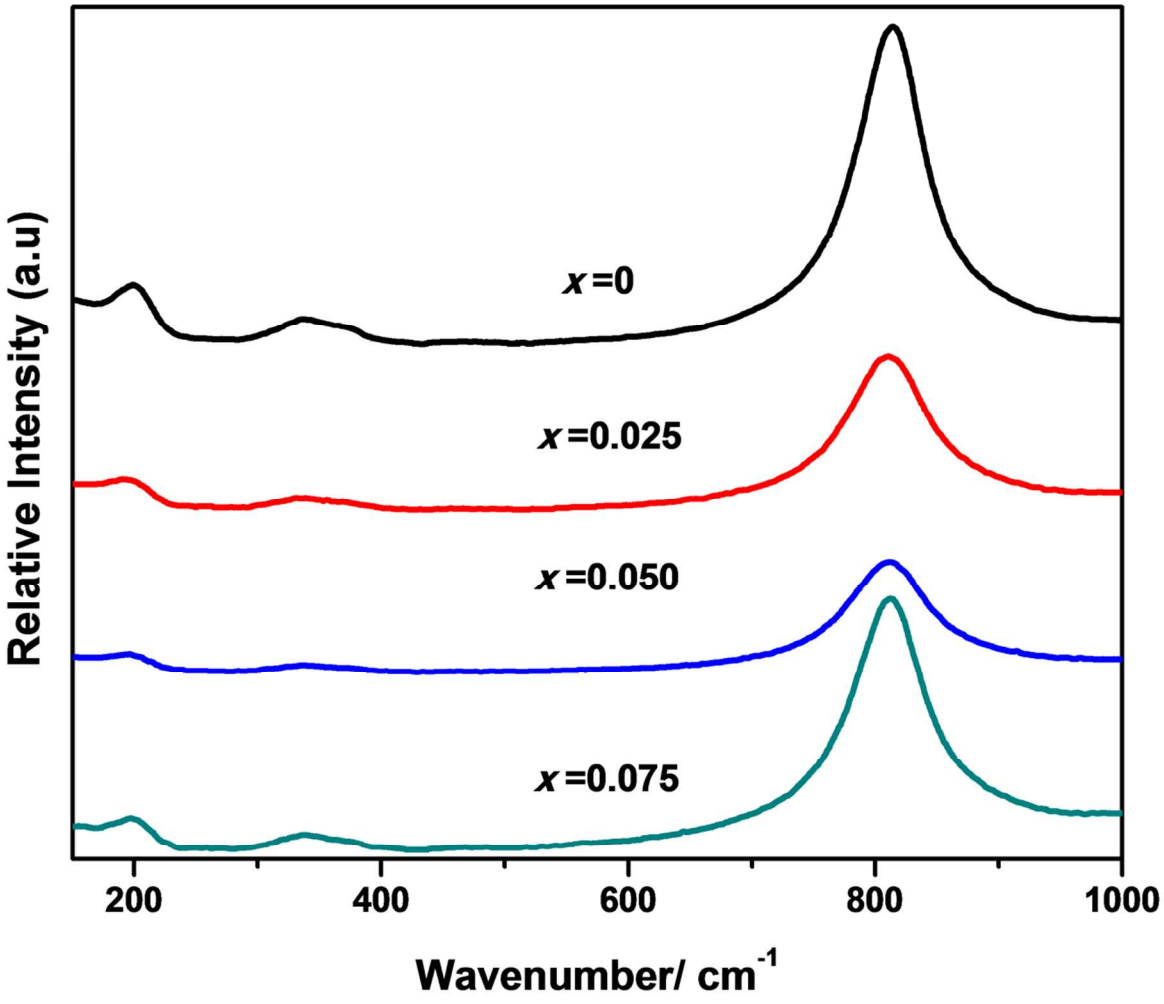

Fig. 3 Raman spectra of $BiV_{1-x}Nb_xO_4$; x = 0, 0.025, 0.05, 0.075 synthesized at 500°C.

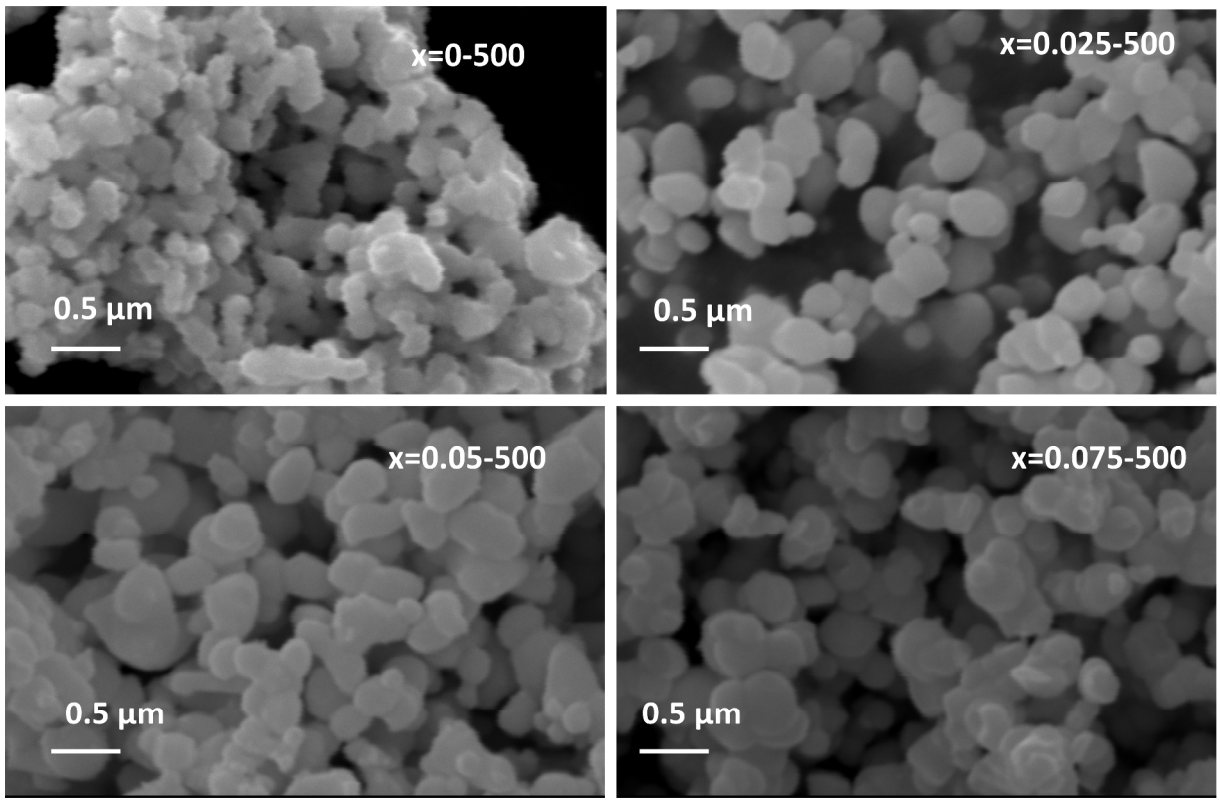

Fig. 4 SEM micrographs of $BiV_{1-x}Nb_xO_4$; x = 0, 0.025, 0.05, 0.075.

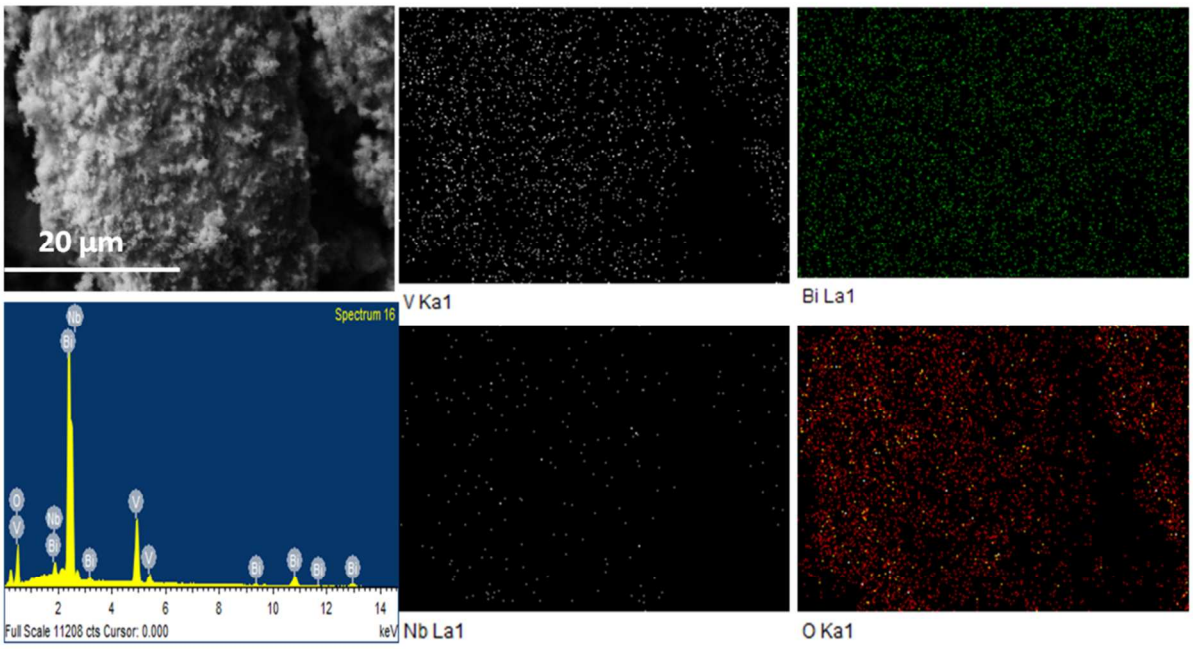

Fig. 5 EDS elemental mapping data of (a) Bi, (b) V, (c) Nb, (O) in $BiV_{0.975}Nb_{0.025}O_4$ sample synthesized at 500°C.

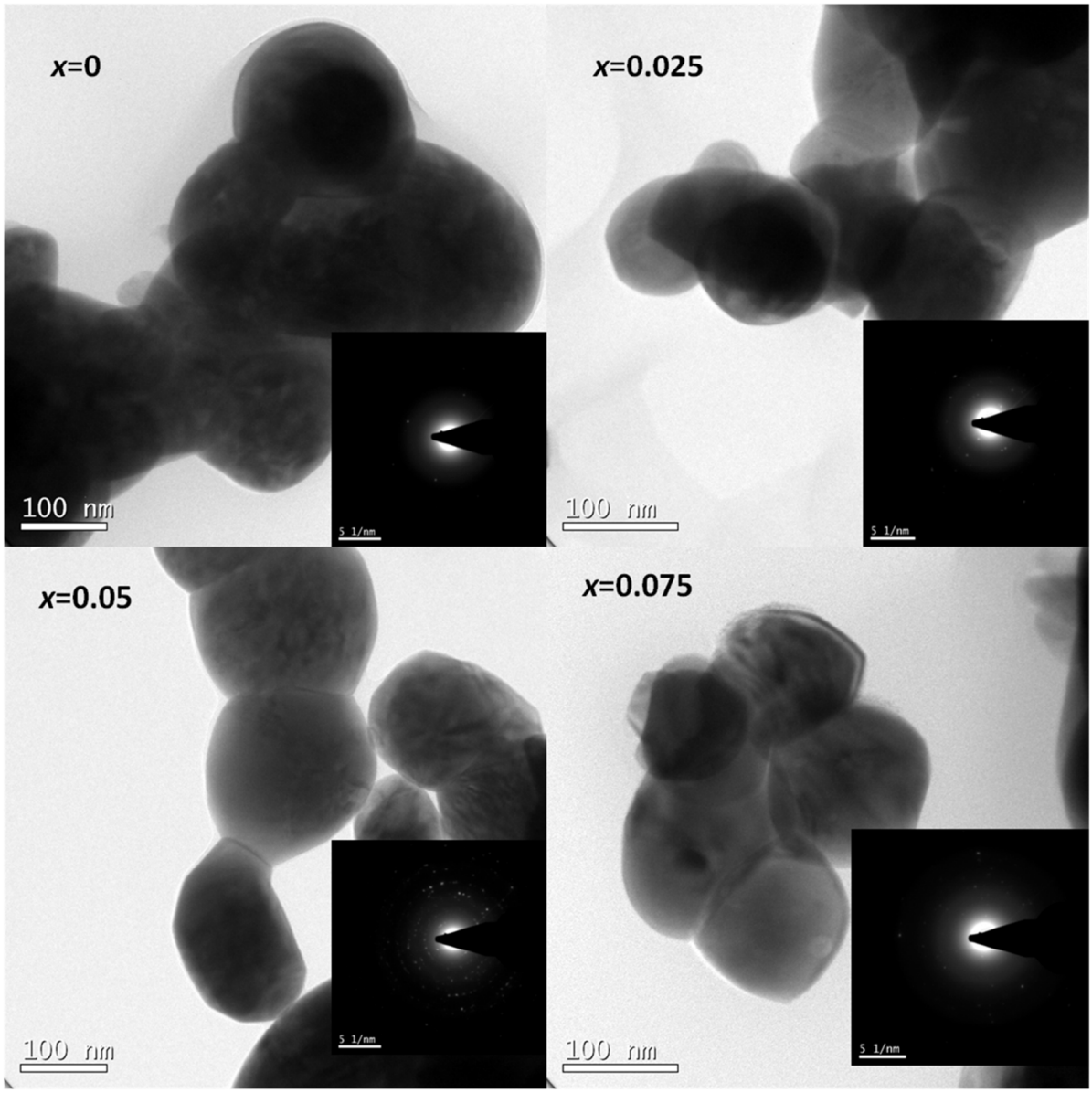

Fig. 6 TEM micrographs of $BiV_{1-x}Nb_xO_4$; x = 0, 0.025, 0.05, 0.075 pigments (SAED patterns inset).

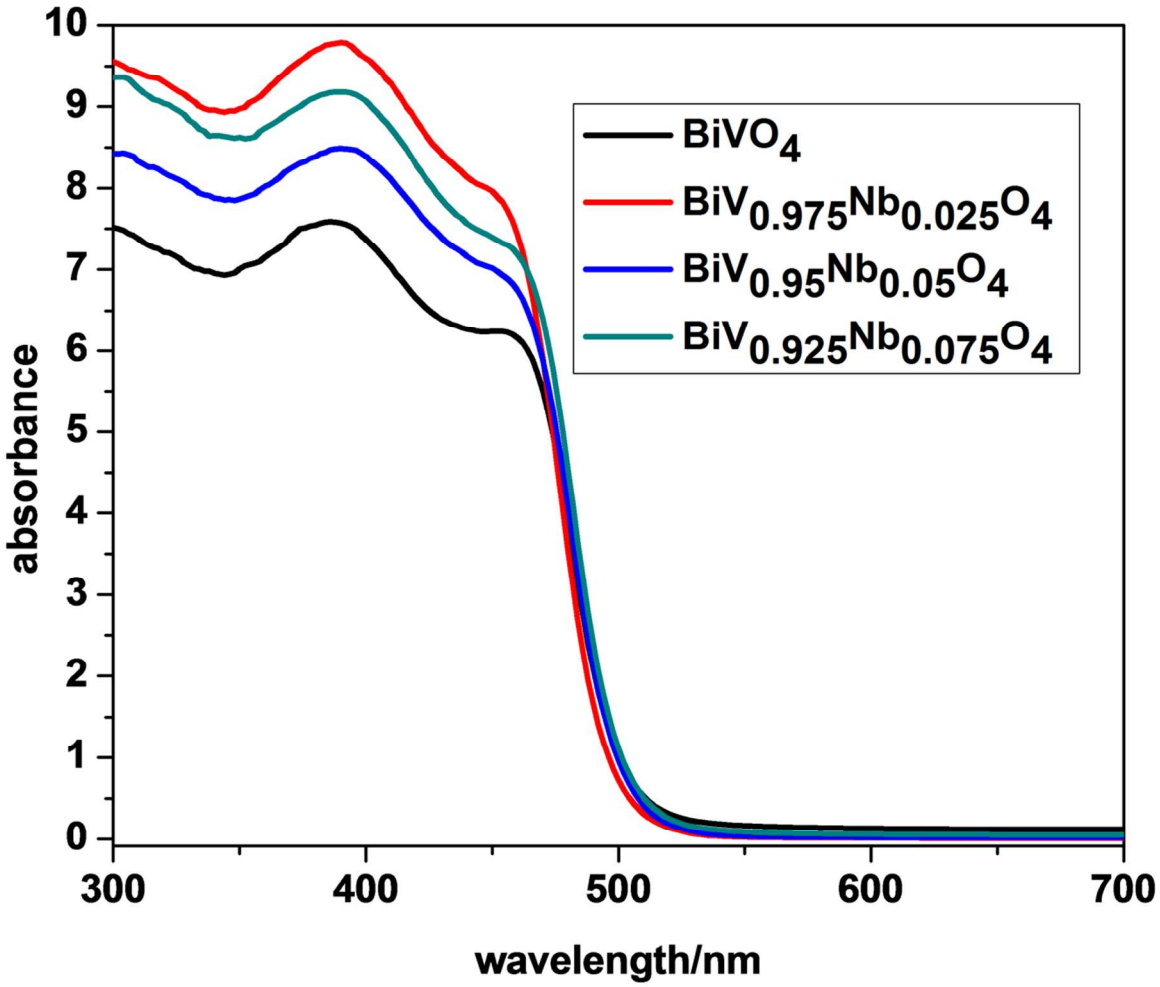

Fig. 7 Absorption spectra of $BiV_{1-x}Nb_xO_4$; x = 0, 0.025, 0.05, 0.075 synthesized at 500°C.

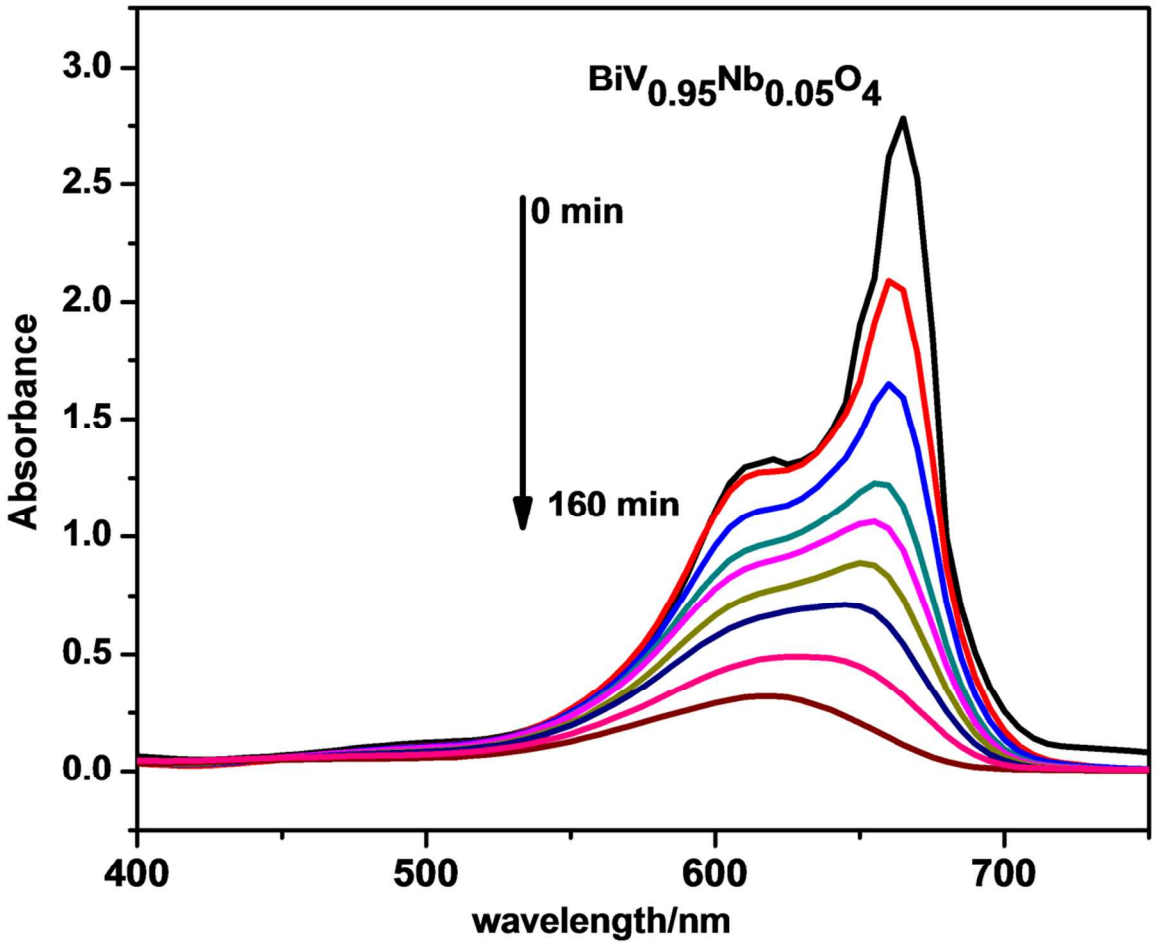

Fig. 8 UV visible spectral changes of MB as a function of irradiation time for $BiV_{0.95}Nb_{0.05}O_4$ sample under sunlight.

Probing Structural Variation and Multifunctionality in Niobium Doped Bismuth Vanadate Materials

Sameera Saithathul Fathimah, Padala Prabhakar Rao, Vineetha James, Athira K. V. Raj, Chitradevi G.R, Sandhyakumari Leela*

Multifunctional materials in $BiV_{1-x}Nb_xO_4$ solid solutions display high NIR reflecting brilliant yellow hues with notable MB dye degradation under sunlight.